http://dx.doi.org/10.17159/2411-9717/2017/v117n10a9

A comparative study of hardness of Pt-Cr-V and Pt-Al-V alloys in the as-cast and annealed conditions

by B.O. Odera*†‡ and L.A. Cornish†‡#

Synopsis

Microhardness values of alloys in the Pt-Cr-V and Pt-Al-V systems were determined using an indenter which incorporated an optical microscope. The values were analysed with respect to the phases identified in each of the alloys. Identification of the phases had been done earlier using scanning electron microscopy with energy dispersive X-ray spectroscopy and X-ray diffraction. The hardness values were determined for samples in the as-cast and annealed conditions and superposed on the solidification projection and isothermal section at 1000°C. The results showed that the hardness depended largely on the phases present in the alloys and generally increased after annealing. However, in a few cases, grain growth and the resulting microstructural coarseness resulted in lower hardness values after annealing. The hardness of the alloys of the Pt-Cr-V and Pt-Al-V systems was also compared with those of Pt-Al-Cr and other Pt-Al based alloys. Comparison was also made with some Pt-Al based alloys of the higher order systems such as Pt-Al-Cr-Ru-V and Pt-Al-Cr-Ru-V-Nb. In general, higher hardness was exhibited by alloys containing ternary phases.

Keywords
Pt-based ternary alloys, Pr-Cr-V, Pt-Al-V, hardness, microstructure.

Introduction

Platinum-based alloys for high-temperature corrosive environments have been investigated as possible replacements for nickel-based superalloys (NBSAs) in the hotter parts of gas turbines (Wolff and Hill, 2000; Hill *et al.*, 2001b). The NBSAs have excellent mechanical properties due to their γ/γ' structure but are limited by their maximum operating temperatures. Currently, the maximum temperature at which NBSAs operate is approximately 1100°C, which is approximately 85% of their melting temperature (Sims, Stoloff and Hagel, 1987). There is a need to develop new alloys that can operate at higher temperatures. The advantages include increased efficiency, which is related to the combustion temperature and higher temperatures would enable greater thrust, improved fuel efficiency and reduced pollution.

Platinum has the same fcc structure and similar chemistry to nickel, as well as a higher melting point (1769°C for platinum, compared to 1455°C for nickel) and better corrosion resistance than nickel (Süss *et al.*, 2003). Alloy development work done by other researchers demonstrated that ternary and quaternary Pt-based alloys can exhibit a γ/γ′ two-phase structure, similar to nickel-based superalloys (Hill *et al.*, 2001; Cornish Fischer and Völkl, 2003). Although the use of Pt-based alloys as a replacement for Ni-based superalloys is limited due to their higher price and higher density, it is possible that they could be used for critical components, or as corrosion-resistant coatings (Süss *et al.*, 2009).

Some of the quaternary alloys exhibiting the γ/γ′ two-phase structure were of the Pt-Al-Cr-Ru system. Alloys of the quinary Pt-Al-Cr-Ru-V system have also been investigated as potential replacement of NBSAs (Odera, 2013; Odera *et al.*, 2015). Vanadium replaced some of the Pt to reduce density and cost, as well as acting as a solid solution strengthener. Pt-Al-V and Pt-Cr-V are two component ternary systems of the quinary and a study of the microstructures of selected alloys of the systems and their ternary phase diagrams formed part of the investigation (Odera *et al.*, 2012b; Odera, 2013; Odera *et al.*, 2014). This paper presents hardness values of selected alloys of the two ternary systems in the as-cast and annealed conditions and compares and discusses these values in relation to the microstructures.

There is an empirical relationship between hardness and strength of a metal. Since hardness testing is easier to perform than

* *Department of Mechanical Engineering, Cape Peninsula University of Technology, Cape Town.*
† *School of Chemical and Metallurgical Engineering, University of the Witwatersrand, Johannesburg.*
‡ *African Materials Science and Engineering Network (AMSEN), a Carnegie-IAS Network.*
\# *DST-NRF Centre of Excellence in Strong Materials, hosted by University of the Witwatersrand, Johannesburg.*

 ISSN 2225-6253. This paper was first presented at the AMI Precious Metals 2017 Conference 'The Precious Metals Development Network' *17–20 October 2017, Protea Hotel Ranch Resort, Polokwane, South Africa.*

tensile strength testing, especially for small samples, it is often used to obtain an indication of the strength of a metal, especially when only small samples are available (Dieter, 1986; Smith, 1990).

Experimental procedure

Twenty-four alloy buttons weighing approximately 2 g each were prepared from Pt, Al, Cr of 99.9% purity and V of 99.6% purity. Out of these, 11 samples identified as Alloy 1 to Alloy 11 were of the Pt-Al-V system, while those identified as Alloy 12 to Alloy 24 were of the Pt-Cr-V system, all in the as-cast condition. The annealed samples were identified as 1H to 11H and 12H to 24H respectively. The samples were manufactured by arc-melting under argon atmosphere on a water-cooled copper hearth with a Ti oxygen-getter. Each button was turned over and re-melted three times in an attempt to achieve homogeneity. The samples were then halved and one half of each was metallographically prepared in the as-cast condition, while the other half was annealed for 1500 hours before preparation.

The samples were ground on silicon carbide down to 1200 grit and then diamond polished down to 1 µm. The samples were then etched in a solution of 10 g NaCl in 100 cm^3 HCl (32% vol. concentration) (Odera *et al.*, 2012a). Etching was done in a fume cupboard using a DC power supply and a voltage range of 9 V to 12 V gave adequate results. The current density in the electrolyte was approximately 100 $A.m^{-2}$. The counter-electrode was a stainless steel wire suspended in the electrolyte solution. The indenter used incorporated an optical microscope with a maximum magnification of 1000 times and only an etched surface could be seen clearly in the machine. In the unetched condition, it was difficult to differentiate between the sample and the mounting resin surface. The hardness of the alloys was measured using a Vickers microhardness tester with a load of 300 g. At least five measurements were carried out to obtain an average hardness value.

Results

Figure 1a shows an indentation on as-cast Alloy 5, average composition $Pt_{83.9}$:Al_6:V10.1 (at.%) and Figure 1b shows an indentation on annealed Alloy 5H of the same average composition. The indentations on as-cast Alloy 24 and annealed Alloy 24H, average composition $Pt_{34.1}$:$Cr_{57.4}$:$V_{8.5}$ are shown in Figure 2. Figures 3 and 4 show indentations on as-cast Alloys 15 and 18, average compositions $Pt_{53.0}$:$Cr_{22.4}$:$V_{24.5}$ and $Pt_{25.8}$:$Cr_{42.9}$:$V_{31.3}$ respectivley. Table I gives hardness values ($HV_{0.3}$) for as-cast and annealed Pt-Al-V alloys, together with the phases in each of the alloys, while Table II gives the same data for Pt-Cr-V alloys.

Discussion

As-cast Alloys of the Pt-Al-V System

Alloys with a Pt content more than 70 at.% had the lowest hardness values (less than 500 $HV_{0.3}$), while 64% of the alloys had relatively high hardness values of more than 500 $HV_{0.3}$. The single-phase ternary Alloy 11 had the highest hardness of 886 $HV_{0.3}$, which would be expected and is likely to be brittle. Generally, the load of 300 g used was too low to cause substantial cracking during indentation on these particular alloys. However, Alloy 11 exhibited cracks before indentation, confirming its brittle nature.

Hill *et al.* (2001a, 2001b) reported Vickers macrohardness measurements on several Pt-based ternary alloys at room temperature. Eight of these were Pt-Al-Z alloys (where Z was Ni, Ru or Re). Six of the alloys had Vickers hardness less than 500 HV in the as-cast and annealed conditions and the highest value was 530 HV (the load used was not specified). In his investigation of Pt-Al-Cr alloys, Süss (2007) found that 75% of the alloys in the as-

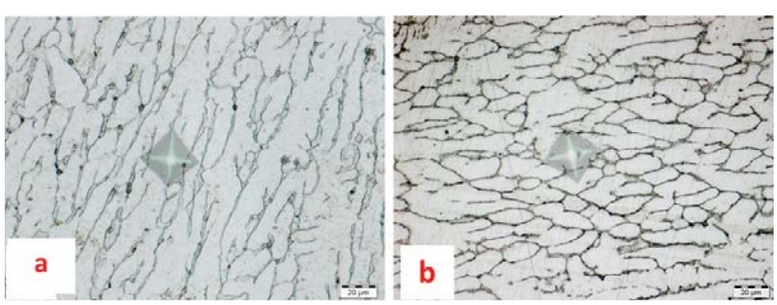

Figure 1—Vickers hardness indentation on (a) as-cast Alloy 5, (b) annealed Alloy 5H, average composition $Pt_{83.9}$:Al_6:$V_{10.1}$ (at.%)

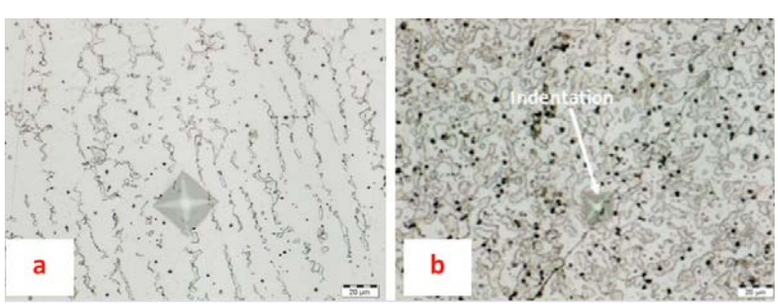

Figure 2—Vickers hardness indentation on (a) as-cast Alloy 24, (b) annealed Alloy 24H, average composition $Pt_{34.1}$:$Cr5_{7.4}$:$V_{8.5}$ (at.%)

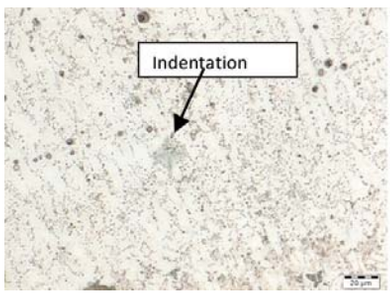

Figure 3—Vickers hardness indentation on as-cast Alloy 15, average composition $Pt_{53.0}:Cr_{22.4}:V_{24.5}$ (at.%)

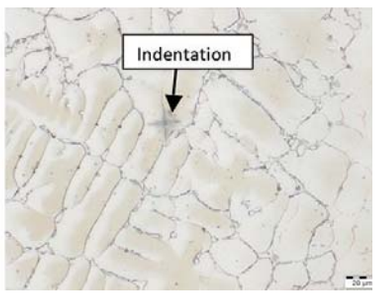

Figure 4—Vickers hardness indentation on as-cast Alloy 18, average composition $Pt_{25.8}:Cr_{42.9}:V_{31.3}$ (at.%)

Table I

Hardness values ($HV_{0.3}$) of annealed Pt-Al-V alloys compared to as-cast alloys

Alloy ID No.	Average composition (at.%)	As-cast hardness ($HV_{0.3}$)	Annealed hardness ($HV_{0.3}$)	Phases present in the as-cast alloys	Phases present in the annealed alloys
1	$Pt_{64.3}:Al_{26.6}:V_{9.1}$	655±27	635±13	~Pt_3Al, ~Pt_5Al_3, ~Pt_2Al, ~Pt_3V, PtAl	~Pt_3Al, Pt_5Al_3, ~Pt_2V, PtAl
2	$Pt_{59.1}:Al_{23.1}:V_{17.8}$	746±35	624±26	~Pt_2V, ~Pt_5Al_3, PtAl	~PtV, ~Pt_5Al_3
3	$Pt_{69.3}:Al_{9.6}:V_{21.1}$	519±34	516±17	~Pt_3V, ~Pt_3Al, ~Pt_2Al	~Pt_2V, ~Pt_3Al, ~PtV
4	$Pt_{69.8}:Al_{22.3}:V_{7.9}$	671±23	696±20	~Pt_3Al, ~Pt_2Al	~Pt_3Al, ~Pt_2Al
5	$Pt_{83.9}:Al_6:V_{10.1}$	420±20	482±14	(Pt), ~Pt_3Al	(Pt), ~Pt_2V, ~Pt_3Al
6	$Pt_{80.9}:Al_{4.3}:V_{14.8}$	381±13	378±16	(Pt), ~Pt_3Al	(Pt), ~Pt_3Al
7	$Pt_{52.5}:Al_{22.6}:V_{24.9}$	767±37	733±18	~PtV, ~PtV_3, ~Pt_5Al_3	~PtV, ~PtV_3, ~Pt_5Al_3
8	$Pt_{53.7}:Al_{8.8}:V_{37.5}$	584±19	585±19	~PtV, ~PtV_3, ~Pt_5Al_3	~PtV, ~PtV_3, ~Pt_5Al_3
9	$Pt_{84}:Al_{12}:V_4$	475±9	347±10	(Pt), ~Pt_3Al	(Pt), ~Pt_3Al
10	$Pt_{72.4}:Al_{13.7}:V_{13.9}$	462±14	535±23	~Pt_3Al, ~Pt_2Al	~Pt_3Al
11	$Pt_{56.9}:Al_{25.4}:V_{17.7}$	886±23	-	τ_2	~PtAl, ~PtV

Table II

Hardness values ($HV_{0.3}$) of annealed Pt-Cr-V alloys compared to as-cast alloys

Alloy ID No.	Average composition (at.%)	As-cast hardness ($HV_{0.3}$)	Annealed hardness ($HV_{0.3}$)	Phases present in the as-cast alloys	Phases present in the annealed alloys
12	$Pt_{73.8}:Cr_{16.9}:V_{9.3}$	272±8	280±26	~Pt_3V	~Pt_3V
13	$Pt_{72.3}:Cr_{8.3}:V_{19.4}$	317±8	330±17	~Pt_3V	~Pt_2V, Pt_3V
14 τ_3	$Pt_{33.4}:Cr_{45.8}:V_{20.8}$	527±28	589±23	~Cr_3Pt, A15(~Cr_3Pt), τ_3	~Cr_3Pt, ~CrPt A15(~Cr_3Pt),
15	$Pt_{53.0}:Cr_{22.4}:V_{24.5}$	936±59	637±28	~CrPt, τ_3	~Cr_3Pt, τ_3
16	$Pt_{68.5}:Cr_{16.2}:V_{15.3}$	291±19	350±8	~Pt_3V	~Pt_3V
17	$Pt_{32.8}:Cr_{28.6}:V_{38.6}$	854±30	1086±46	~Cr_3Pt, τ_3	~Pt_2V, τ, ~CrPt
18	$Pt_{25.8}:Cr_{42.9}:V_{31.3}$	1109±25	-	τ_3, A15(~Cr_3Pt), ~Cr_3Pt	A15(~Cr_3Pt), ~Cr_3Pt, τ_3
19	$Pt_{38.8}:Cr_{14.2}:V_{47.0}$	796±35	923±57	~PtV_3, ~PtV, τ_3	~PtV_3, ~PtV, τ_3
20	$Pt_{16.8}:Cr_{13.4}:V_{69.8}$	618±25	-	(V,Cr), ~PtV_3	(V,Cr), ~PtV_3
21	$Pt_{28.7}:Cr_{27.2}:V_{44.1}$	1086±28	-	~Cr_3Pt, ~PtV_3, τ_3, (V,Cr)	~PtV_3 τ, (V,Cr)
22	$Pt_{16.5}:Cr_{56.1}:V_{27.4}$	707±41	837±46	(V,Cr), A15(~Cr_3Pt)	(V,Cr), A15(~Cr_3Pt)
23	$Pt_{14.9}:Cr_{73.7}:V_{11.4}$	692±73	544±20	(V,Cr), A15(~Cr_3Pt)	(V,Cr), A15(~Cr_3Pt)
24	$Pt_{34.1}:Cr_{57.4}:V_{8.5}$	358±9	838±27	~Cr_3Pt, A15(~Cr_3Pt)	~Cr_3Pt, A15(~Cr_3Pt)

cast condition had Vickers hardness over 600 HV_{10} at room temperature.

Figure 5 shows hardness values of as-cast Pt-Al-V alloys superimposed on the partial solidification projection at the Pt-rich corner derived and reported by Odera (2013). It shows the hardness values increasing away from the Pt-rich corner. The composition of the two ternary phases τ_1 and τ_2 are approximately $V_{24}Pt_{56}Al_{20}$ and $V_{18}Pt_{57}Al_{25}$ respectively.

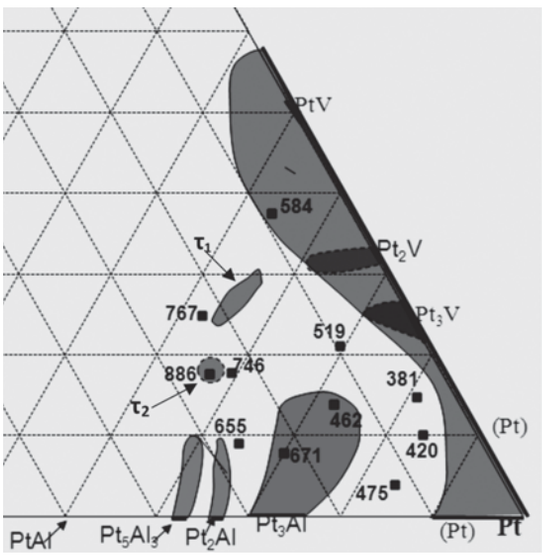

Figure 5—Hardness values ($HV_{0.3}$) of as-cast Pt-Al-V alloys superimposed on the solidification projection (at.%)

Pt-Al-V alloys annealed at 1000°C for 1500 Hours

The hardness values for annealed alloys of the Pt-Al-V system are given in Table III. Seventy per cent of the annealed alloys had hardness values higher than 500 HV and the rest, which had relatively high Pt contents above 80 at.%, had hardness values below 500 $HV_{0.3}$. About 45% of the alloys had hardness values over 600 $HV_{0.3}$. Annealed Alloy 11H cracked and disintegrated while being ground in preparation for polishing and etching, indicating that it was very brittle and it also contained the ternary phase in as the-cast condition. In all of the alloys, there was no cracking or noticeable deformation around the indentations, therefore their toughness could not be quantitatively assessed. However, the absence of notable cracking suggests reasonable toughness (except for Alloy 11 which comprised the ternary phase in the as-cast condition and had cracks before indentation). However, this could also be attributed to the relatively small load used in the microhardness testing. The small load was chosen because of the small size of the samples (approx. 1 g). However, these hardness values for the alloys, whether in the as-cast or annealed condition, are very high compared to that of pure platinum, which is very soft and ductile with a Vickers hardness of 50 HV (the load was not specified) (Murakami, 2008).

These results are comparable to the findings of Süss (2007) in his investigation of Pt-Al-Cr alloys, where just over half of the annealed alloys had hardness values above 600 HV_{10}. Only one of the Pt-Al based alloys, Pt_{62}:Al_{19}:Ni_{19}, investigated by Hill (2001) had a hardness value of 530 HV (the load used was not specified). The rest had hardnesses below 500 HV.

The phase ~Pt_2Al disappeared during annealing of Alloy 1H, but the hardness remained more or less the same. In Alloy 2H, two phases, ~Pt_2V and ~PtAl, disappeared and a new phase, ~PtV, formed while ~Pt_5Al_3 was present both in the as-cast and annealed conditions. The hardness of Alloy 2H reduced by approximately 100 $HV_{0.3}$, suggesting that one or both of the two phases that disappeared contributed to the higher hardness in the as-cast condition.

The hardness of Alloys 3 and 4 remained more or less the same after annealing. In Alloy 3, the two phases ~Pt_3V and ~Pt_2Al disappeared and two new phases, ~Pt_2V and ~PtV, formed while in Alloy 4 there was no change in the phases.

In Alloy 5, a new phase, ~Pt_2V, formed during annealing, while the two phases (Pt) and ~Pt_3Al were retained. There was a slight increase of hardness from 420±20 $HV_{0.3}$ to 482±14 $HV_{0.3}$, suggesting that the new phase was responsible for the increase, as expected. The phases in Alloy 6 remained the same and, as expected, the hardness was also similar after annealing.

The hardness of Alloys 7 and 8 remained the same after annealing if the standard deviations are taken into account. This is not surprising as the phases ~PtV, ~PtV_3 and ~Pt_5Al_3 remained the same before and after annealing.

The hardness of Alloy 9 decreased by approximately 100 HV, while the two phases (Pt) and ~Pt_3Al remained the same in the as-cast and annealed conditions. The decrease in hardness may be explained by coarsening of the phases during annealing. Alloy 10 changed from two-phase ~Pt_3Al + ~Pt_2Al to single phase ~Pt_3Al, while the hardness increased from 462±14 $HV_{0.3}$ to 535±23 $HV_{0.3}$. This suggests that ~Pt_2Al is a soft phase compared to ~Pt_3Al and its disappearance contributed to the increase in hardness.

Alloy 11 consisted of a single ternary phase, τ2 and was the hardest alloy, even in the as-cast condition, with Vickers hardness of 886±23 $HV_{0.3}$. Further evidence of its hardness and brittleness were the visible cracks around the indentation in the as-cast condition. It disintegrated while being removed from the resin mount and so it was not possible to measure the hardness in the annealed condition.

Figure 6 shows hardness values superimposed on isothermal section of Pt-Al-V at 1000°C, at the Pt-rich corner as derived and reported earlier (Odera *et al.*, 2014). The same trend is seen as with the as-cast alloys, where the hardness values reduced with increasing Pt content.

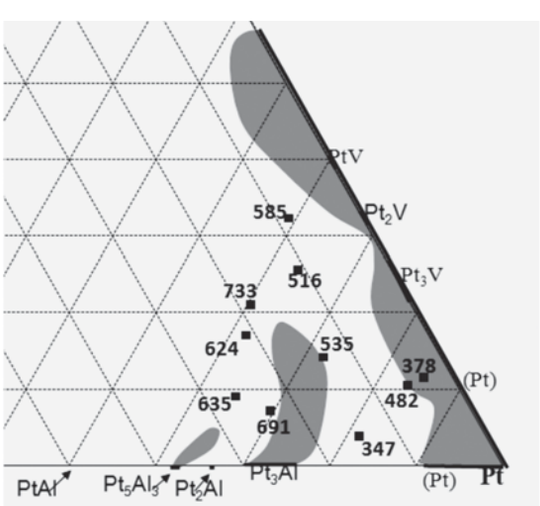

Figure 6—Hardness values ($HV_{0.3}$) of annealed Pt-Al-V alloys superposed on the isothermal section at 1000°C (at.%)

As-cast Pt-Cr-V alloys

The alloys having ternary phase dendrites (Alloys 17, 18 and 21) had very high hardness values, as expected. Alloy 18 had the highest hardness value (1109±25 $HV_{0.3}$). The second hardest alloy was Alloy 21, which had a hardness of 1086±28 $HV_{0.3}$. All the indentations on Alloy 15 were on the eutectic areas and the high hardness value of 936±59 $HV_{0.3}$ reflects the high hardness of the ternary phase component of the eutectic, rather than the binary intermetallic component. The single-phase Alloys 12 and 13, which had high Pt contents, had the lowest hardness values. Alloy 16, which also had high Pt content, had a similarly low hardness. The rest of the alloys all had relatively high hardness values, except for Alloy 24 which had a low hardness value of 358±19 $HV_{0.3}$.

The hardness values were comparable to those obtained by Süss (2007) in his investigation of Pt-Al-Cr alloys. Süss (2007) used a load of 10 kg and many of the alloys cracked and deformed around the indentations. However, the highest Vickers hardness values obtained by Süss (2007) were between 800 HV_{10} and 900 HV_{10}. The hardness of the Pt-Cr-V alloys investigated in this work were also generally much higher than the ternary Pt-Al based alloys investigated by Hill *et al.* (2001) which had a maximum hardness value of 530 HV (the load used was not specified). These hardness values for the alloys, whether in the as-cast or annealed condition, were much higher than for pure platinum, which is very soft and ductile with a Vickers hardness of approximately 50 HV (Murakami ,2008).

Figure 7 shows hardness values superimposed on the solidification projection of the Pt-Cr-V system. It shows that alloys having high Pt content have the lowest hardness and there is an increase in hardness as one moves away from the Pt-rich corner.

Pt-Cr-V alloys annealed at 1000°C for 1500 hours

There was a general increase in hardness values after annealing the Pt-Cr-V alloys, except for Alloys 15H and 23H, which had lower values and this was probably due to microstructure coarsening. Alloys 17, 18 and 21 (as-cast) had ternary phase dendrites with high hardness values in the as-cast condition, as expected. These three alloys also exhibited extreme brittleness. The annealed Alloys 18H and 21H cracked and disintegrated while being removed from the resin mounting. Alloy 18H cracked, but stayed as one piece and therefore it was possible to undertake microhardness tests. The annealed Alloy 20H also cracked and disintegrated while being removed from the resin mounting. The alloys with high Pt content had the lowest hardness values.

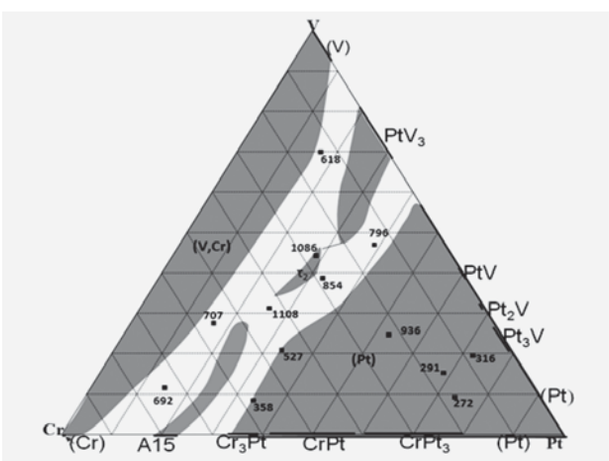

Figure 7—Hardness values ($HV_{0.3}$) of as-cast Pt-Cr-V alloys superimposed on the solidification projection (at.%)

If the three annealed alloys that disintegrated are included among those with hardness values exceeding 600 $HV_{0.3}$, then approximately 62% of the alloys had Vickers hardnesses higher than 600 $HV_{0.3}$. This shows that the alloys were generally harder than those investigated by Süss (2007), just over half of which had Vickers hardnesses higher than 600 HV_{10}. Again, if the same three alloys are included among those that had hardness values higher than 750 $HV_{0.3}$, then slightly more than half the alloys had hardness values more than 750 $HV_{0.3}$ compared to those investigated by Süss (2007), only three of which (17%) had hardness values higher than 750 HV_{10}. The assumption that the three alloys that disintegrated had hardness values higher than 750 $HV_{0.3}$ is valid because the hardest annealed alloy whose hardness was measured is Alloy 18H (1086 $HV_{0.3}$) and an other three alloys had hardness values exceeding 800 $HV_{0.3}$. These alloys were much harder than the Pt-Al based alloys investigated by Hill (2001), the hardest of which had a Vickers hardness of 530 HV (the load used was not specified).

The hardness of Alloys 12H and 13H remained similar after annealing. Alloy 12H remained single phase ~Pt_3V after annealing, while Alloy 13H changed from a single phase structure of ~Pt_3V to a two-phase structure of ~Pt_2V and ~Pt_3V. This shows that the two phases ~Pt_2V and Pt_3V have similar hardness. Alloy 16H, which was also single phase ~Pt_3V in the as-cast condition, retained the same phase after annealing, with a slight increase in hardness. This is probably due to traces of (Pt) detected by XRD in the as-cast alloy but which disappeared after annealing.

The phases in Alloy 14H were the same before and after annealing and there was not much change in the hardness, as expected. However, there was a substantial decrease in the hardness of Alloy 15H after annealing, although the phases were the same. This decrease is attributed to coarsening.

In Alloy 17H, the phase ~Cr_3Pt disappeared and ~Pt_2V formed after annealing, while the ternary phase, τ_3, was present both in the as-cast and annealed conditions. The increase in hardness from 854±30 $HV_{0.3}$ to 1085±46 $HV_{0.3}$ is therefore attributed to ~Pt_2V, as expected. Alloy 18, which had the highest hardness value at 1109±25 $HV_{0.3}$ in the as-cast condition, disintegrated while being removed from the resin mounting after SEM analysis following annealing, therefore its hardness was not measured. However, the phases, τ_3, A15(~Cr_3Pt) and ~Cr_3Pt, remained the same in the as-cast and annealed conditions and the disintegration indicated extreme hardness and brittleness of the alloy.

The phases in Alloy 19H did not change after annealing, but the hardness increased from 796±35 $HV_{0.3}$ to 923±57 $HV_{0.3}$. This was the same with Alloy 20H, where the phases (V,Cr) and ~PtV_3 remained the same in the as-cast and annealed conditions. However, Alloy 20H disintegrated while being removed from the resin mounting and it was not

possible to measure its hardness after annealing, although the disintegration suggested extreme hardness and brittleness.

Alloy 21 had a hardness value of 1086±28 $HV_{0.3}$, making it the second hardest alloy in the as-cast condition. It had the same phases ~Cr_3Pt, ~PtV_3, τ_3 and (V,Cr) in the as-cast and annealed conditions. It disintegrated while being removed from the resin mounting and as such, its annealed hardness was not measured. The disintegration indicated extreme hardness and brittleness. The phases, (V,Cr) and A15(~Cr_3Pt), in Alloy 22H remained the same in the as-cast and annealed conditions, but the hardness increased from 707±41 $HV_{0.3}$ to 837±46 $HV_{0.3}$.

Alloy 23H had the same phases, (V,Cr) and A15(~Cr_3Pt) in the as-cast and annealed conditions, but the hardness decreased from 692±73 $HV_{0.3}$ to 544±20 $HV_{0.3}$. This deviated from the trend seen for most of the alloys in this system. Alloy 24H also retained the same phases, ~Cr_3Pt and A15 (~Cr_3Pt), in the as-cast and annealed conditions, but there was a substantial increase in hardness from 358±9 $HV_{0.3}$ to 838±27 $HV_{0.3}$. This was because heat treatment produced more of the A15 (~Cr_3Pt), which would be expected to be harder, being an intermetallic phase.

Figure 8 shows hardness values superposed on the isothermal section at 1000°C derived by and reported in Odera (2013). Hardness is lowest at the Pt-rich corner and increases with reduction in Pt content.

Figure 9 shows a combined plot of hardness values of as-cast and annealed Pt-Al-V alloys, while Figure 10 shows a similar plot for Pt-Cr-V alloys. There is a general increase in hardness values for the Pt-Cr-V alloys after annealing, while there is little change in the values for Pt-Al-V alloys.

Comparison with higher order alloys

Table III shows the $HV_{0.3}$ hardness values of higher order Pt-based alloys (Odera *et al.*, 2015). Pt-Al-V and Pt-Cr-V alloys were generally much harder than the as-cast higher order alloys, because many of the Pt-Al-V and Pt-Cr-V alloys contained hard Pt-V intermetallic phases. The high hardness of some of the Pt-Al-Cr alloys (Süss, 2007) was attributed to ~$PtAl_2$, ~PtAl and ~Pt_2Al_3.

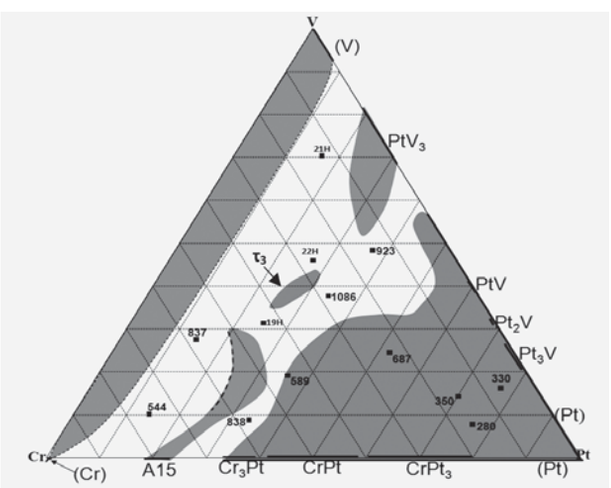

Figure 8—Hardness values ($HV_{0.3}$) of annealed Pt-Cr-V alloys superposed on the isothermal section at 1000°C (at.%)

Conclusions

Microhardness values for selected Pt-Al-V and Pt-Cr-V alloys were determined in the as-cast and annealed conditions. Alloys with high Pt content (more than 70 at.%) had the lowest hardness values, while those containing ternary phases had the highest hardness. The single ternary phase Alloy 11 (average composition $Pt_{56.9}$:$Al_{25.4}$:$V_{17.7}$) had the highest hardness of 886±23 $HV_{0.3}$ among the Pt-Al-V alloys in the as-cast condition. Alloy 18 (average composition $Pt_{25.8}$:$Cr_{42.9}$:$V_{31.3}$) had the highest hardness value of 1109±25 $HV_{0.3}$ among the Pt-Cr-V alloys in the as-cast condition. These two sets of alloys, especially the Pt-Cr-V alloys, had higher hardness values than the Pt-Al-Cr alloys studied by Süss (2007) and Pt-Al based alloys studied by Hill *et al.* (2001), as well as the high-order Pt-based alloys studied by Odera *et al.* (2015).

References

Cornish, L.A., Fischer, B. and Völkl, R. 2003. Development of platinum-group-metal superalloys for high-temperature use. *MRS Bulletin*, vol. 28, no. 9. pp. 632–638.

Dieter, G.E. 1986. *Mechanical Metallurgy*. 3rd edn. McGraw-Hill, New York. pp. 329–330.

Hill, P.J., Cornish, L.A., Ellis, P. and Witcomb, M.J. 2001a. The effects of Ti and Cr additions on the phase equilibria and properties of (Pt)/Pt_3Al alloys. *Journal of Alloys and Compounds*, vol. 322, no. 1. pp.166–175.

Hill, P.J., Biggs, T., Ellis, P., Hohls, J., Taylor S.S. and Wolff, I.M. 2001b. An assessment of ternary precipitation-strengthened Pt alloys for ultra-high temperature applications. *Materials Science and Engeering A*, 301, pp. 67–179.

Murakami, T., Sahara, R., Harako, D., Akiba, M., Narushima, T. and Ouchi, C. 2008. The effect of solute elements on hardness and grain size in platinum based binary alloys. *Materials Transactions*, vol. 49, no. 3. pp. 538–547.

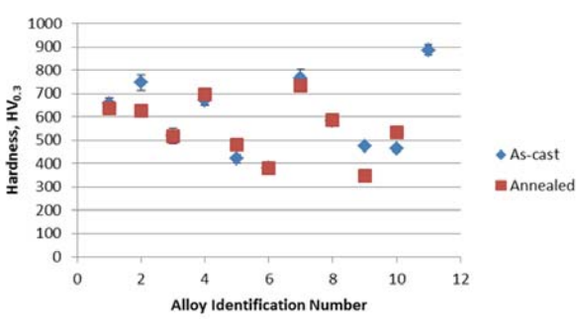

Figure 9—Combined hardness plot of as-cast and annealed Pt-Al-V alloys

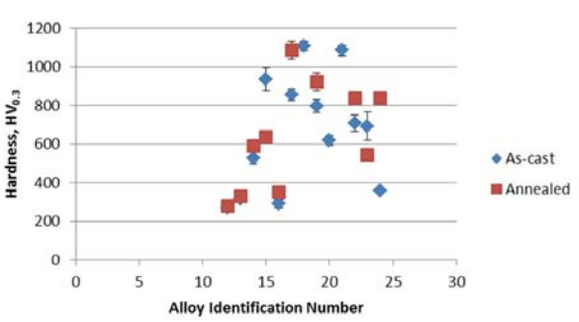

Figure 10—Combined hardness plot of as-cast and annealed Pt-Cr-V alloys

Table III

Hardness values of as-cast and annealed higher order (Odera *et al.*, 2015) alloys

Alloy ID No.	Average composition (at.%)	As-cast hardness ($HV_{0.3}$)	Annealed hardness ($HV_{0.3}$)	Phases present in the as-cast alloys	Phases present in the annealed alloys
1 and 1H	$Pt_{63.9}:Al_{12.2}:Cr_{4.3}:Ru_{0.7}:V_{18.9}$	537±13	700±20	~Pt_3Al, (Pt)	~Pt_3Al, ~Pt_2V
2 and 2H	$Pt_{69.5}:Al_{11.5}:Cr_{4.2}:Ru_{0.6}:V_{14.2}$	428±11	482±24	~Pt_3Al, (Pt)	~Pt_3Al
3 and 3H	$Pt_{75.2}:Al_{11.2}:Cr_{4.0}:Ru_{0.6}:V_{9.5}$	377±8	359±9	~Pt_3Al	~Pt_3Al
4 and 4H	$Pt_{78.7}:Al_{12.2}:Cr_{3.8}:Ru_{0.6}:V_{5.2}$	422±9	-	~Pt_3Al	~Pt_3Al, (Pt)
5 and 5H	$Pt_{63.2}:Al_{12.9}:Cr_{4.0}:Ru_{0.7}:V_{19.0}:Nb_{0.6}$	603±21	821±32	~Pt_3Al, (Pt)	~Pt_3Al, ~PtV, ~Pt_2V
6 and 6H	$Pt_{71.7}:Al_{12.8}:Cr_{4.9}:Ru_{1.1}:V_{9.9}:Nb_{0.3}$	545±12	535±15	~Pt_3Al, (Pt)	~Pt_3Al

Odera, B.O. 2013. Addition of vanadium and niobium to platinum-based alloys. PhD thesis, University of the Witwatersrand, Johannesburg.

Odera, B.O., Cornish, L.A., Papo, M.J. and Rading, G.O. 2012a. Electrolytic etching of platinum-aluminium based alloys. *Platinum Metals Review*, vol. 56, no. 4. pp. 257–261.

Odera, B., Cornish, L.A., Shongwe, M.B., Rading, G. and Papo, M.J. 2012b. As cast and heat-treated alloys of the Pt-Al-V system at the Pt-rich corner. *Journal of the Southern African Institute of Mining and Metallurgy*, vol. 112, no. 7. pp. 505–516.

Odera, B., Papo, M.J., Rading, G. and Cornish, L.A. 2014. Experimental solidification projection, liquidus surface projection and isothermal section at 1000° C for the Pt-Cr-V system. *Journal of Phase Equilibria and Diffusion*, vol. 35, no. 4. pp. 476–489.

Odera, B., Papo, M.J., Couperthwaite, R., Rading, G., Billing, D. and Cornish, L.A. 2015. High-order additions to platinum-based alloys for high-temperature applications. *Journal of the Southern African Institute of Mining and Metallurgy*, vol. 115, no. 3. pp. 241–250.

Sims, C.T., Stoloff, N.S. and Hagel, W.C. 1987. *High-temperature Materials for Aerospace and Industrial Power*. Wiley, New York. Süss, R., Cornish, L.A., Hill, P.J., Hohls, J. and Compton, D.N. (2003). Properties of a new series of superalloys based on $Pt_{80}:Al_{14}:Cr_3:Ru_3$. *Advanced Materials and Processes for Gas Turbines*, pp. 301–307.

Süss, R. 2007. Investigation of the Pt-Al-Cr system as part of the development of the Pt-Al-Cr-Ru thermodynamic database. PhD thesis, University of the Witwatersrand, Johannesburg.

Süss, R., Watson, A., Cornish, L.A. and Compton, D.N. 2009. Development of a database for the prediction of phases in Pt–Al–Cr–Ru alloys for high-temperature and corrosive environments: Al–Cr–Ru. *Journal of Alloys and Compounds*, vol. 476, no. 1. pp. 176–186. ◆

http://dx.doi.org/10.17159/2411-9717/2017/v117n10a10

Alternative carbon materials as practical and more durable fuel cell electrocatalyst supports than conventional carbon blacks

by M.L. Stevenson and G. Pattrick

Synopsis

Conventional low-temperature proton exchange membrane fuel cell (LTPEMFC) electrocatalyst supports suffer from excessively high corrosion rates. In this work, several alternative carbons were investigated in terms of their viability to produce 'drop-in' alternative electrocatalysts to the conventional materials while providing significantly enhanced support corrosion resistance. This was to establish their potential to serve both current and future markets. The materials examined were: partially graphitised Vulcan, a hierarchical porous graphene-like material and commercial graphitised carbon nanofiberes (CNFs). Samples were prepared at 40 wt% Pt loading and performance compared to conventional Pt (40wt%)/Vulcan and Pt (40wt%)/Ketjenblack. CNFs were the only material to display improved corrosion resistance over the conventional supports. The catalyst did, however, suffer from comparatively low beginning-of-life performance. This work did nonetheless demonstrate good promise for the commercial CNF support in producing functional electrocatalysts that could (a) potentially be directly substituted into well-established conventional catalyst-based MEA manufacturing processes and (b) offer considerably enhanced support corrosion resistance.

Keywords
PEM fuel cell, electrocatalyst support, corrosion, carbon nanfibres, durability.

Introduction

Conventional electrocatalysts supported on Vulcan XC72R and Ketjenblack EC300J display poor durability under typical automotive operating conditions, as well as certain stationary applications (Zhang, 2008; Gasteiger, Vielstich and Lamm, 2003; Rabis, Rodriguez and Schmidt, 2012). This leads to fuel cell stack lifetimes far lower than current targets set by the US Department of Energy (5000 hours for automotive; 40 000 hours for stationary) (US Department of Energy, 2013). Two major degradation mechanisms, particularly on the cathode, are responsible for this: instability in the nanometre-sized Pt particles on the catalysts and corrosion of the carbon support material (Gasteiger, Vielstich and Lamm, 2003). Both of these mechanisms lead to losses in active area and, as a result, losses in catalytic activity of the materials. Corrosion of the support also reduces the porosity of the electrode catalyst layers, decreasing the accessibility of reagent gases to the active sites on the catalyst (Schulenburg *et al.*, 2011).

Typically, systems-level measures are incorporated into the fuel cell stack design to prevent modes of operation which are particularly damaging to the support (Zhang, 2008; Gasteiger, Vielstich and Lamm, 2003). Carbon corrosion does nevertheless occur and so to further improve the useful life of the membrane electrode assembly (MEA), catalysts supported on materials with inherently higher corrosion resistance are needed.

Conventional supports possess several properties essential for high performance catalyst layers within MEAs (Rabis, Rodriguez and Schmidt, 2012), which alternative carbons would also need to maintain:

- High electronic conductivity, in excess of 1 S/cm. This is needed to keep electronic resistance (ohmic) losses in the catalyst layer to a minimum
- High specific surface area, in the region of 50 to 800 m^2/g, to achieve high dispersions of the active Pt metal. This is to maximise the utilisation of the catalyst
- Ability to form a structure with high porosity when fabricated into catalyst layers. This is essential for creating a large three-phase interfacial area in the electrodes of an MEA.

Increasing the graphitic content of a carbon material is a common technique to improve its stability. Yu *et al.*, (2006) reported that with *in situ* testing, an MEA fabricated using a catalyst supported on a graphitised carbon black showed a degradation rate five times lower than that of an MEA made with a standard carbon-black-supported catalyst. This was after 1000 start/stop cycles – a degradation protocol particularly taxing to a carbon support.

* *HySA/Catalysis, South African Council for Mineral Technology, Mintek, South Africa.*

ISSN 2225-6253. This paper was first presented at the AMI Precious Metals 2017 Conference 'The Precious Metals Development Network' *17–20 October 2017, Protea Hotel Ranch Resort, Polokwane, South Africa.*

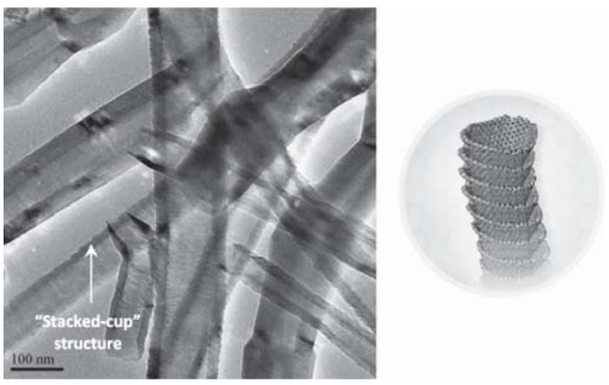

Figure 1— Left: HRTEM image of as-received Pyrograf PR-24-XT-HHT carbon nanofibres. Right: Computer-generated representation of 'stacked-cup' structure of the nanofibres (source: http://pyrograf-products.com, accessed 15 December 2016)

Highly graphitised carbon materials other than carbon black are also being investigated as viable alternative supports. In particular, graphitised carbon nanofibres and nanotubes have shown promise in producing catalysts with high metal dispersions and improved support corrosion resistance over the standard carbon blacks (Guha, Zawodzinski and Schiraldi, 2008; Lee *et al.*, 2006; Zaragoza-Martin *et al.*, 2007).

Another key consideration of this work, however, was to establish whether certain alternative supports would be capable of providing enhanced support corrosion benefits for both current and future applications. Since many existing large-scale MEA manufacturing processes are currently based on conventional catalysts, viable alternative carbons would need to produce electrocatalysts directly compatible with these processes to see rapid entry into current commercial pipelines.

The alternative carbons examined were: a partially graphitised form of Vulcan XC72R (pG-Vulcan) produced by Cabot®; highly graphitised carbon nanofibres (CNFs) from Pyrograph® Products, Inc. (PR-24-XT-HHT); and a 3D network, hierarchical porous graphene-like material (HPG) obtained through international collaborations within the HySA/Catalysis programme.

Experimental

Catalyst preparation

Catalysts were prepared according to a proprietary synthesis technique developed within the HySA/Catalysis programme. In brief, the routine involved the precipitation of Pt complexes from an aqueous solution of Pt precursor, followed by deposition on to the carbon support material and *in situ* reduction with a suitable reducing agent. Syntheses in per batch quantities from 0.5 g to 1 kg per batch have been thoroughly investigated and shown to yield Pt/C materials supported on Vulcan XC72R and Ketjenblack EC-300J without any losses in performance throughout the scale-up procedure.

Ex-situ catalyst characterisation

X-ray Diffraction

XRD was used to characterise the crystallographic structure of selected catalyst samples. Co K radiation was used and scans were performed from 10° to 120° (2θ) using a Bruker D8 Advance diffractometer. Average Pt crystallite sizes were calculated using the Scherrer equation applied to the Pt(220) diffraction peak (Venkateswara Rao and Viswanathan, 2010).

HRTEM

High-resolution TEM images, using a JEOL JEM-2100F instrument, were taken of selected catalyst samples to visualise metal dispersions, for validation of the Pt surface areas predicted by cyclic voltammetry and also the average crystallite sizes calculated from XRD.

BET surface area

BET surface area measurements were performed on the various support materials using a Micromeritics ASAP 2020. All samples were degassed at 350°C under vacuum for 4 hours prior to measurement.

Thin-film rotating disk electrode measurements

All TF-RDE measurements were performed in 0.1M HClO4 using a three-electrode cell. A saturated calomel electrode (SCE) served as reference and a Pt strip as counter-electrode. All reported potentials were referenced back to the relative hydrogen electrode (RHE). The working electrode was a 5 mm glassy carbon RDE and all measurements were carried out on an Autolab PGSTAT302N potentiostat.

Prior to the measurements, the glassy carbon electrodes were polished with 0.05 µm alumina on a Buehler Texmet® polishing pad. Catalyst inks were prepared by dispersing a calculated mass of catalyst in approximately. 15 mℓ of high-purity water by ultrasonication for 30 minutes. Catalyst was then deposited at a Pt loading density of 56 µg m^2 after which 27.8 µL of a 0.2817 mg/mL Nafion® solution was micropipetted on top of the catalyst layer and dried in an oven at 120°C for 10 minutes.

Pt surface area measurements were performed in N_2-purged, 0.1M $HClO_4$, maintained at 25°C. The catalyst layers on the RDEs were first conditioned by cycling the potential between 0 and 1.2 V_{RHE} at 50 mV/s for 15 cycles. Thereafter, three further cycles were measured at 20 mV/s and the hydrogen adsorption charge of the third cycle used to calculate the Pt surface area of the catalyst. In order to limit contributions from molecular hydrogen evolution, integration for the hydrogen adsorption charge was performed up until the potential of the current maximum following the Pt(111) adsorption peak in the cathodic sweep. A specific charge transfer value of 210 µC/cm^2 Pt was assumed.

Kinetic ORR activity measurements were carried out in O_2-saturated electrolyte at 60°C. The RDE was rotated at 1600 r/min and the potential was swept from 0 to 1.0 V_{RHE} at 20 mV/s. Background correction to remove the capacitive currents not related to ORR was performed in N_2-purged electrolyte at 60°C with zero rotation of the RDE. Mass transport limitations were removed using the Koutecky-Levich equation (Gasteiger *et al.*, 2005) and a Tafel analysis performed on the kinetic data between 875 and 950 m V_{RHE}.

Pt particle stability was assessed by cycling the potential between 0.6 and 1.0 V_{RHE} for 7200 square-wave cycles, with Pt SA measured at 1200-cycle intervals. This was done in N_2-purged 0.1M $HClO_4$ at 60°C. Support corrosion resistance was evaluated by holding the potential on the RDE at 1.5 V_{RHE} for

2 hours and then averaging the final 2 minutes of the measurement to obtain a measure of the support corrosion current. This was performed in N_2-purged, 25°C $HClO_4$.

In situ evaluation

MEA fabrication

Catalyst-coated substrates (CCS) with active areas of 50 cm^2 were fabricated by a procedure developed within HySA/Catalysis. Catalyst inks were prepared using a proprietary combination of solvents, catalyst and 15 wt% ionomer solution (IonPower™, LQ-1015). An I:C ratio of 0.75 was employed for both the anode and cathode catalyst layers. A Silverson® L5MA high-sheer mixer was used to homogenise the ink components before transfer to a USI® Prism 300 spray coater. Catalyst layers were then deposited onto Freudenberg H2315 I2C6 GDLs by ultrasonic spray coating and dried in an oven at 120°C for 30 minutes. Targeted electrode Pt loadings were 0.4/0.4 mg Pt/cm^2 (anode/cathode). The resulting gas diffusion electrodes (GDEs) were hot-pressed onto opposite sides of Nafion® NRE211 membrane at a pressure of 10 MPa relative to active area, at 135°C for 3 minutes.

Testing protocols

Prior to evaluation, newly fabricated MEAs were subjected to a conditioning protocol in order to stabilize performance at the assembly's peak value. This involved cycling the potential on the MEA between 1.0 V (or open circuit) for 30 seconds and 0.3 V for 10 minutes. This was performed for a total of 12 cycles under the conditions summarised in Table I.

Following this, the MEA was assessed by a number of standard *in situ* testing protocols, the conditions for which are also contained in Table I.

Results and discussion

Ex-situ analysis

Figure 2 displays a comparison of the BoL thin-film RDE cyclic voltammograms measured on the catalysts synthesised with the various supports. Included are the CVs obtained on the conventional Pt(approx. 40 wt%)/Vulcan XC72R (HySA-V40) and Pt(approx. 40 wt%)/Ketjenblack EC-300J (HySA-K40) materials. Table II summarises the Pt loadings, BoL Pt surface areas and kinetic ORR activities measured on the various catalyst samples and Table III provides a comparison of the Pt particle sizes determined by TF-RDE, XRD and HRTEM. Also shown in Table III are the BET surface areas measured on the supports.

What is immediately apparent in Figure 2 is the extremely low initial metal area measured on the CNF-supported catalyst relative to the other Pt (approx. 40 wt%) materials. At just 35.8 m^2/g Pt, this represents only 41% of the metal area obtained on the standard Vulcan-supported HySA-V40. The TF-RDE Pt surface area ranking on the catalysts, as well as the XRD Pt crystallite and HRTEM Pt particle sizes in general, followed the BET surface areas measured on the supports, with lower BET SAs yielding lower Pt SAs. This is unsurprising, as smaller support surface areas relate to a lower number of active sites on the support for metal deposition, leading to a lower Pt dispersions for a given synthesis procedure.

Table I

Summary of testing conditions used for MEA evaluation

Parameter	Conditioning	Polarisation Curve/ CTR @ 100 mA/cm^2	Kinetic ORR Activity	Cathode EPSA/ Hydrogen Crossover
A/C Feed Gas	Hydrogen/Air	Hydrogen/Air	Hydrogen/Oxygen	Hydrogen/Nitrogen
A/C Feed Flow Rates	2.0 x Stoich. at 1600 mA/cm^2	1.5/2.0	2.0/4.0 NL/min	0.5/0.5 NL/min
A/C Back Pressure	2.0/2.0 bar(abs)	2.0/2.0 bar(abs)	1.0/1.0 bar(abs)	1.0/1.0 bar(abs)
A/C Feed Gas Temp.	90/90 °C	90/90 °C	90/90 °C	90/90 °C
A/C Feed Humidity	100/80% RH	100/80% RH	100/100 %RH	100/100 %RH
Cell Temp.	80°C	80°C	80°C	80°C

Table II

Summary of Pt loadings and BoL TF-RDE measurements performed on catalysts supported on the various carbon materials

Sample Name	Support	Scale of Synthesis (g)	Pt Loading (wt%)	Pt SA from H_{ads} (CV) (m^2/g Pt)	Kinetic ORR Activities @ 900mV *vs.* RHE		
					Tafel Slope (mV/dec)	Specific (µA/cm^2 Pt)	Mass (A/mg Pt)
HySA-V40 (FCU4007)	Vulcan XC72R	50	37.58 ±0.08	87.4 ±0.9	66.4 ±0.8	220 ±5	0.192 ±0.005
HySA-K40 (FCKU4007)	Ketjenblack	50	42.18 ±0.14	110.2 ±4.7	62.8 ±1.3	152 ±9	0.168 ±0.006
FCHPG4002	HPG	7	40.02	97.9 ±6.1	70.3 ±2.1	189 ±12	0.186 ±0.022
FCGV4001	pG-Vulcan	7	38.78 ±0.14	75.5 ±5.3	66.2 ±2.9	258 ±47	0.193 ±0.023
FCNF4003	CNFs	7	38.30 ±0.12	35.8 ±0.5	64.7 ±0.6	324 ±20	0.116 ±0.008

Table III

Comparision of Pt particle/crystallite sizes determined by TF-RDE, XRD and HRTEM on the various catalyst samples, along with the BET surface areas measured on the supports

Sample Name	Support	BET SA (m^2/g Support)	Avg. Pt Particle/Crystallite Size		
			TF-RDE (nm)	XRD (nm)	HRTEM (nm)
HySA-V40 (FCU4007)	Vulcan XC72R	237.1	3.2	3.3	2 - 4
HySA-K40 (FCKU4007)	Ketjenblack	850.6	2.5	2.7	2 - 3
FCHPG4002	HPG	581.3	2.9	3.6	2 - 4
FCGV4001	pG-Vulcan	147.9	3.7	-	2 - 4
FCNF4003	CNFs	44.7	7.8	4.6	3 - 5

The average metal particle size calculated from the TF-RDE Pt SA on the Pt/CNF catalyst was 7.8 nm. HRTEM imaging of the catalyst, however, displayed a high dispersion of the Pt metal across the nanofibres with Pt particle sizes typically in the 3 to 5 nm range (Figure 3). In agreement with this is the average Pt(220) crystallite size estimated from XRD, which was 4.6 nm (Figure 4). The reason for the large disparity between these measurements on the CNF-supported catalyst could be the possibility of Pt particle growth inside the nanofibre tubes during synthesis, which may have been inaccessible to the electrolyte during RDE measurements.

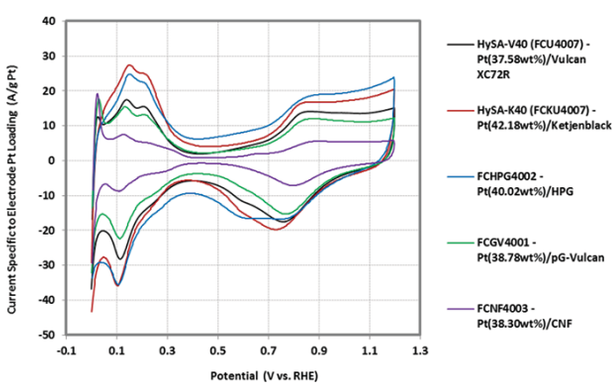

Figure 2—BoL TF-RDE CVs measured on the conventional Pt(approx. 40 wt%)/Vulcan XC72R and Pt(approx. 40 wt%)/Ketjenblack EC-300J catalysts compared to those supported on HPG, CNF and pG-Vulcan

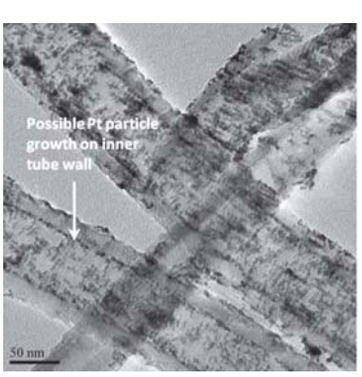

Figure 3—HRTEM image of the Pt (approx. 40 wt%)/CNF catalyst

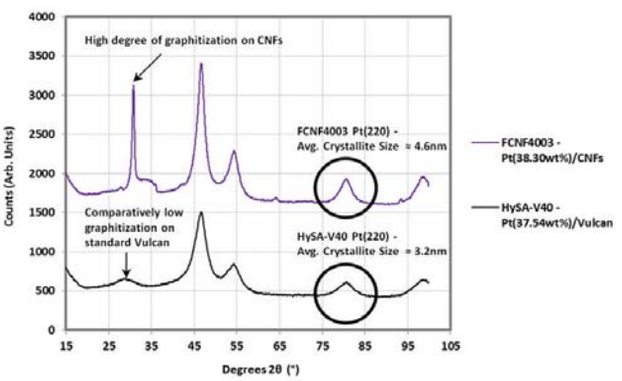

Figure 4—X-ray scans obtained for the Pt(38.30 wt%)/CNF and standard Vulcan-supported HySA-V40 catalyst

HRTEM images appear to confirm this, showing a clear line of Pt metal particles along the inner wall of the CNFs (Figure 3).

In terms of kinetic ORR activity measurements, specific activity was approximately 47% higher on the Pt(38.30 wt%)/CNF sample than the HySA-V40, but because of the very low Pt SA, mass activity was only 60% of the standard Vulcan-supported catalyst at 0.116 A/mg Pt.

Moving on to the Pt(40.02wt%)/HPG catalyst, as can be seen in Table II, it possessed an initial Pt surface area between that of the HySA-V40 and HySA-K40 catalysts at 97.9 m^2/g Pt. In agreement with this, HRTEM imaging of the catalyst indicated particles in the 2-4 nm range. Kinetic ORR mass activity was found to be essentially the same as the HySA-V40. BoL performance of the HPG supported catalyst therefore seemed very promising, matching that of the conventional catalysts.

The pG-Vulcan-supported catalyst showed a Pt surface area only marginally lower than the conventional HySA-V40. Kinetic ORR mass activity was also on par with the HySA-V40 with, however, a slightly higher specific activity at 900 m V_{RHE}, attributed to the larger average Pt particle size on the pG-Vulcan-supported material. This was possibly due to the Pt particle size effect.

Being referred to here is the straightforward relationship between Pt particle size and ORR activity, where larger particles have been associated with higher specific activities and lower mass activities and smaller particles associated with smaller specific activities and higher mass activities

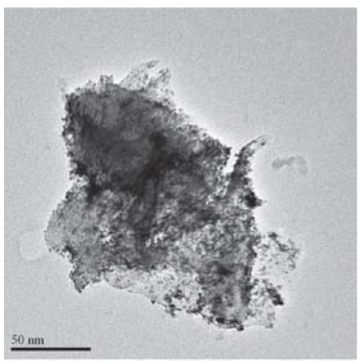

Figure 5—HRTEM image of the Pt(approx. 40wt%)/HPG catalyst

(Gasteiger *et al.*, 2005). The drop-off in mass activity with increasing Pt particle size has been found to increase somewhat only at values below approximately 60-70 m^2/g Pt (Gasteiger *et al.*, 2005). Thus with sample FCGV4001 possessing approximately 75.5 m^2/g Pt, the impact on mass activity of its slightly larger particles on average than the HySA-V40 was perhaps not seen because of this phenomenon.

Looking now at durability testing, Figure 6 presents the Pt surface area decay profiles obtained from the thin-film RDE Pt stability ADT. As can be seen, with the exception of the HPG-supported catalyst, all the materials actually showed fairly similar degradation profiles, losing between 35 and 42% of their initial Pt surface area by the end of the test. The HPG-supported catalyst clearly showed the highest degradation, however, losing nearly 60% of its active area by the end of the ADT.

The CNF- and pG-Vulcan supported catalysts performed only as good as their standard Vulcan-and Ketjenblack-supported counterparts and so improved support durability would be the only potential advantage the alternative carbons could offer over the conventional carbon blacks.

Figure 7 displays the corrosion currents measured over the final 1200 seconds of the TF-RDE support corrosion resistance ADT. In terms of the alternative carbons, the HPG-supported catalyst showed the highest corrosion current, which was in fact 10% higher than the Pt(approx. 40 wt%)/Ketjenblack material. Showing both lower Pt particle stability and support corrosion resistance, the HPG material did not appear to have any improved durability over the conventional carbon blacks and therefore would likely not provide any significant advantage over these materials.

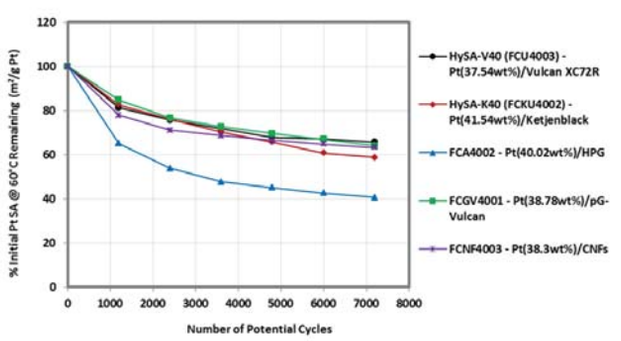

Figure 6—Pt surface area degradation profiles measured by the TF-RDE Pt stability ADT

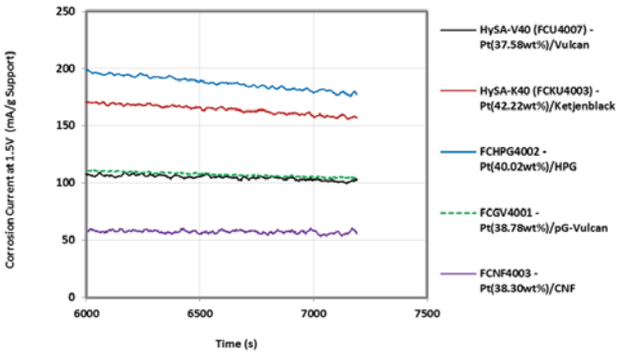

Figure 7—Corrosion currents measured by the TF-RDE support corrosion resistance ADT

The partially graphitised Vulcan-supported catalyst, rather surprisingly, showed essentially the same average corrosion current as the HySA-V40. It was anticipated that the graphitisation imparted into the material, however small, would at least provide a noticeable enhancement in support corrosion resistance. With respect to the TF-RDE BoL and ADT measurements, therefore, the pG-Vulcan material was almost indistinguishable from standard Vulcan, except in terms of BoL Pt SA, for which it showed a 14% reduction. It was thus expected that it would show no appreciable advantage over the HySA-V40 in a fuel cell environment either and with the material costing more than standard Vulcan, it would in fact be less attractive as a fuel cell catalyst support.

In situ analysis and Pt(approx. 20 wt%)/CNF catalyst

The CNF-supported catalyst was the only material to show any improvement in support corrosion resistance over the conventional carbon blacks. The improvement was in fact fairly substantial, with the two-minute average corrosion current approximately 36 and 63% lower than the HySA-V40 and HySA-K40 catalysts, respectively. Unfortunately, this improved support corrosion resistance came at the cost of a large reduction in BoL Pt dispersion and kinetic ORR activity.

In view of these results, it was decided to investigate lowering the Pt loading on the CNF supported catalyst to 2 0wt%. Table IV summarises a comparison between the BoL TF-RDE measurements performed on the 20 and 40 wt% Pt/CNF catalysts, as well as the HySA-V20 and V40 materials.

As can be seen, the 20 wt% Pt/CNF catalyst did indeed show an increase in Pt SA by approximately 60% over the 40 wt% material, achieving just under 60 m^2/g Pt *versus* the 35.8 m^2/g Pt of sample FCNF4003. Rather surprisingly, kinetic ORR mass activity was actually somewhat lower, at around 0.095 A/g Pt, compared to 0.115 A/gPt for the 40 wt% catalyst. A near 50% reduction in specific activity appeared to be the cause for this and thus a phenomenon besides the Pt particle size effect was likely at play.

As can be seen in the HRTEM images of Figure 8, there appeared yet again to be a significant deposition of Pt particles on the inner nanofibre walls of the Pt(approx. 20 wt%)/CNF catalyst. A possibility therefore exists that a larger fraction of the total metal may have been inactive on the 20 wt% catalyst than the 40 wt%, resulting in the apparent lower mass activity measured on the material.

Table IV

Comparison of the Pt metal loadings and thin-film RDE measurements of Pt SA and kinetic ORR activity obtained on the Pt(approx. 20 wt%)/CNF and Pt(approx. 40 wt%)/CNF catalysts

Sample Name	Support	Scale of Synthesis (g)	Pt Loading (wt%)	Pt SA from H_{ads} (CV) (m^2/g Pt)	Kinetic ORR Activities @ 900 mV *vs.* RHE		
					Tafel Slope (mV/dec)	Specific (μA/cm^2 Pt)	Mass (A/mg Pt)
HySA-V20 (FCU2002)	Vulcan XC72R	50	18.27 ±0.58	109.4 ±10.4	62.6 ±0.1	196 ±6	0.214 ±0.015
HySA-V40 (FCU4007)	Vulcan XC72R	50	37.58 ±0.08	87.4 ±0.9	66.4 ±0.8	220 ±5	0.192 ±0.005
FCNF4003	CNFs	7	38.30 ±0.12	35.8 ±0.5	64.7 ±0.6	324 ±20	0.116 ±0.008
FCNF2001	CNFs	14	18.71	58.8 ±6.7	65.4 ±1.9	165 ±33	0.096 ±0.013

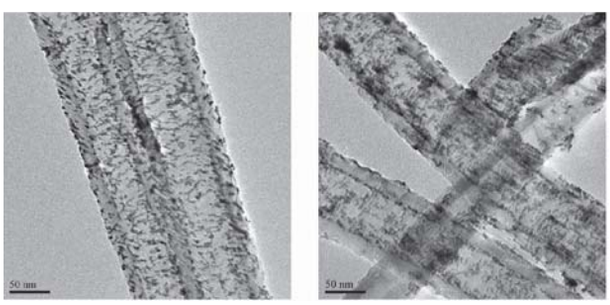

Figure 8—HRTEM images of the 20 wt% (left) and 40 wt% Pt/CNF (right) catalysts

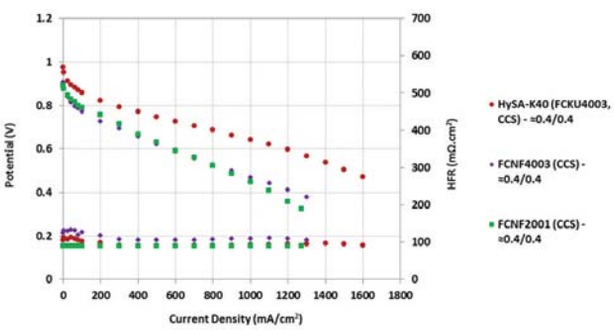

Figure 9—Comparison between the H_2/air polarisation curve and HFR measurements performed on the 50 cm^2 CCSs made with the HySA-K40 and the Pt(18.71 wt%) and Pt(approx. 38.30 wt%) CNF-supported catalysts

Shown in Figure 9 is a comparison of the H_2/air polarisation curves measured on the Pt/CNF- and HySA-K40-based MEAs. Immediately apparent is the drastically lower performance of the CNF-supported catalysts compared to the benchmark HySA-K40 catalyst across the entire range of current densities measured. At 0.6 V, both the 20 and 40 wt% Pt/CNF materials displayed current densities less than half that of the HySA-K40, achieving approximately 570 mA/cm^2 *versus* 1188 mA/cm^2 on the conventional catalyst. A number of possible causes for this are evident in Table V, where, in particular, the *in situ* kinetic ORR mass activities measured on samples FCNF2001 and FCNF4003 were only 13 and 16% of the value obtained on the HySA-K40.

What can also be seen is that the slope in the ohmic region of the polarisation curves for the CNF-based MEAs was higher than for the HySA-K40. Since the HFR values were similar for the MEAs across the range of current densities, it is likely that increased mass transport resistance in the Pt/CNF based layers was the cause for this, having a greater effect on polarisation performance at lower current densities than in the conventional catalyst.

Validation for the increased mass transport resistance is provided by a comparison between the maximum current densities produced – the Pt/CNFs only achieving 1300 mA/cm^2 *vs.* 1600mA/cm^2 for the HySA-K40. A reason for this could have been that the catalyst layer structure produced by the nanofibres had a smaller porosity than the Ketjenblack catalyst, increasing the resistance to diffusion of the reagent gases to the active sites and leading to a lower overall three-phase interfacial area. The bulk density of the CNF material was also noted as being exceptionally lower than that of Ketjenblack and it is therefore likely that the electrode catalyst layers were also appreciably thicker, resulting in poorer gas transport through the layers.

Also apparent was a lower OCV on the Pt/CNF CCSs. Although the exact reason for this is unclear, it may have simply been related to the poorer ORR kinetics on the Pt/CNF cathode catalyst layers. In line with the poorer ORR kinetics was the charge transfer resistance at 100 mA/cm^2, which was also higher on the CNF-based MEAs and cathodic EPSAs were 31 and 65% below that of the HySA-K40 for the 20 and 40 wt% CNF catalysts, respectively.

Conclusions

Several alternative carbon materials were investigated in this work for their viability as replacement supports with improved durability over the conventional Vulcan XC72R and Ketjenblack EC-300J materials. BoL thin-film RDE measurements on samples synthesised at the 40 wt% Pt loading revealed that the HPG and pG-Vulcan catalysts had similar kinetic ORR mass activity at 900 mVRHE as the benchmark conventional catalysts. The Pt(approx. 40 wt%)/CNF catalyst, however, presented only 41% and 60% respectively of the Pt SA and kinetic ORR activity of the Pt(approx. 40 wt%)/Vulcan material.

TF-RDE support corrosion resistance testing indicated that the HPG-supported catalyst had a corrosion current higher than both the V40 and K40 catalysts. Pt stability was also drastically lower, ruling out the material as a valuable, more durable replacement for the conventional carbon blacks. The pG-Vulcan catalyst presented essentially the same corrosion current as the V40; however, the CNF support showed a substantial decrease over the conventional materials, with a corrosion current approximately 63% below the HySA-K40.

Table V

BoL *in situ* performance metrics obtained on the 50 cm² CCSs made with the HySA-K40, Pt(18.71 wt%)/CNF and Pt(38.30 wt%)/CNF catalysts

Metric	HySA-K40 (FCKU4003, CCS) - ≈0.4/0.4	FCNF4003 (CCS) - ≈0.4/0.4	FCNF2001 (CCS) - ≈0.4/0.4
Catalyst	FCKU4003 (Pt(42.22wt%)/KB)	FCNF4003 (Pt(38.30wt%)/CNF)	FCNF2001 (Pt(18.71wt%)/CNF)
Electrode Pt Loadings (anode/cathode, mg Pt/cm²)	0.4/0.4	0.4/0.4	0.4/0.4
Membrane	NRE211	NRE211	NRE211
Gas Diffusion Layer	Freud. C6	Freud. C6	Freud. C6
H2/air Pol. Curve - Current Density @ 0.6V (mA/cm²)	1188	570	576
H2/air Pol. Curve - Peak Power Density (mW/cm²)	756	490	451
H2/air Pol. Curve - HFR @ 1000mA/cm² (mΩ.cm²)	92	108	90
Charge Transfer Resistance @ 100mA/cm² (mΩ.cm²)	530	693	893
ORR Kinetic Activity:			
Tafel Slope >850mV (mV/dec)	76	66	62
Mass Activity @ 900mV (A/mg Pt)	0.137	0.018	0.022
Specific Activity @ 900mV (μA/cm² Pt)	477	181	110
EPSA of Cathode (m²/g Pt)	29	10	20
Hydrogen Crossover (mA/cm²)	2.82	2.48	6.67

To address the extremely poor BoL performance, the Pt loading on the CNF supported catalyst was reduced from 40 to 20 wt%. This, as expected, resulted in an increase in BoL Pt SA by nearly 60%, but with no corresponding improvement in kinetic ORR mass activity. This was proposed to be the result of Pt particles being deposited on the inner tube walls of the CNF material, with a larger fraction of the total Pt metal occurring on the inner walls of the Pt(20 wt%)/CNF sample.

In situ H_2/air polarisation curve performance was appreciably lower on both the 20 and 40 wt% Pt/CNF catalysts compared to the HySA-K40. The most significant reasons for this appeared to be *in situ* kinetic ORR mass activity, which was less than 20% of the value measured on the Ketjenblack-supported catalyst, as well as suspected higher mass transport resistance

The CNF catalysts did, however, produce functional electrocatalyst layers showing modest performance without any modification of the MEA manufacturing procedure developed specifically for conventional Vulcan- and Ketjenblack-supported catalysts. There does therefore appear to be some promise for the CNFs in being able to produce electrocatalysts that could function as drop-in replacements for the conventional catalysts. In doing so, they could benefit not only future applications, but current applications as well.

A deeper consideration of the surface properties of the supports and resulting catalysts (microscopic and macroscopic structures, effects on the interparticle distance between the Pt particles of the catalysts, *etc.*) may also help in further elucidating the various phenomena observed in terms of both the *ex-situ* and *in situ* measurement of the various supports. This was beyond the scope of this work, but may be addressed in a follow-up at a later stage.

Acknowledgements

The authors would like to thank the South African Department of Science and Technology (DST) for funding this research through the HySA/Catalysis programme. We would also like to thank Professor Pei Kang Shen from the Advanced Energy Materials Laboratory at the Sun Yat-Sen University of China for providing the hierarchical porous graphene sample material.

References

Carter, R..N., Kocha, S.S., Wagner, F.T., Fay, M. and Gasteiger, H.A. 2007. Artefacts in measuring electrode catalyst area of fuel cells through cyclic voltammetry. *ECS Transactions*, vol. 11, no. 1. pp. 403–410.

Gasteiger, H.A, Vielstich, W. and Lamm, A. 2003. *Handbook of Fuel Cells – Volume 3: Fuel Cell Technology and Applications.* Wiley, Chichester, UK.

Gasteiger, H.A., Kocha, S.S., Sompalli, B. and Wagner, F.T. 2005. Activity benchmarks and requirements for Pt, Pt-alloy and non-Pt oxygen reduction catalysts for PEMFCs. *Applied Catalysis B: Environmental*, vol. 56, no. 1-2. pp. 9–35.

Guha, A., Zawodzinski, T.A. and Schiraldi, D.A. 2008. Influence of carbon support microstructure on the polarization behavior of a polymer electrolyte membrane fuel cell membrane electrode assemblies. *Journal of Power Sources,* vol. 195, no. 16. pp. 5167–5175.

Lee, K., Zhang, J., Wang, H. and Wilkinson, D.P. 2006. Progress in the synthesis of carbon nanotube- and nanofiber-supported Pt electrocatalysts for PEM fuel cell catalysis. *Journal of Applied Electrochemistry*, 36 (5), pp. 507–522.

Li, Y., Li, Z. and Shen, P. 2013. Simultaneous formation of ultrahigh surface area and three-dimensional hierarchical porous graphene-like networks for fast and highly stable supercapacitors. *Advanced Materials*, vol. 25 no. 17. pp. 2474–2480.

Rabis, A., Rodriguez, P. and Schmidt, T. 2012. Electrocatalysis for polymer electrolyte fuel cells: recent achievements and future challenges. *ACS Catalysis*, vol. 2, no. 5. pp. 864-890.

Schulenburg, A., Schwanitz, B., Linse, N., Scherer, G.G., Wokaun, A. and Krbanjevic, J. 2011. Quantification of platinum deposition in polymer electrolyte fuel cell membranes. *Electrochemistry Communications*, vol. 13 no. 9. pp. 921–923.

US Department of Energy. 2013. Fuel cell technical team roadmap. http://energy.gov/sites/prod/files/ 2014/02/f8/ fctt_roadmap_june2013.pdf [accessed 15 December 2016].

Venkateswara Rao, C. and Viswanathan, B. 2010. Monodispersed platinum nanoparticle supported carbon electrodes for hydrogen oxidation and oxygen reduction in proton exchange membrane fuel cells. *Journal of Physical Chemistry C,* vol. 114, no. 18. pp. 8661–8667.

Yu, P.T., Gu, W., Makharia, R., Wagner, F.T. and Gasteiger, H.A. 2006. The impact of carbon stability on PEM fuel cell startup and shutdown voltage degradation. *ECS Transactions*, vol 3, no. 1. pp. 797–809.

Zaragoza-Martin, F., Sopeña-Escario, D., Morallòn, E. and Salinas-Martínez de Lecea, C. 2007. Pt/Carbon nanofibers electrocatalysts for fuel cells: effect of the support oxidizing treatment. *Journal of Power Sources,* vol. 171, no. 2. pp. 302–309.

Zhang, J. 2008. *PEM Fuel Cell Electrocatalysts and Catalyst Layers,* Springer-Verlag, London, UK. ◆